eprints@whiterose.ac.uk
https://eprints.whiterose.ac.uk/

Accepted Manuscript

From Solvent-Free Microspheres to Bioactive Gradient Scaffolds

Morteza Rasoulianboroujeni MSc, Mostafa Yazdimamaghani MSc, Payam Khoshkenar MSc, Venkata Raveendra Pothineni PhD, Kwang Min Kim PhD, Teresa A. Murray PhD, Jayakumar Rajadas PhD, David K. Mills PhD, Daryoosh Vashaee PhD, Keyvan Moharamzadeh PhD, Lobat Tayebi PhD
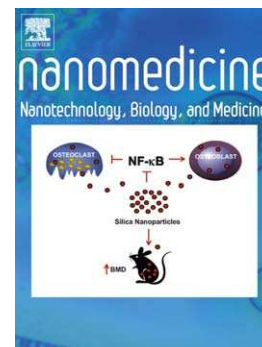
Please cite this article as: Rasoulianboroujeni Morteza, Yazdimamaghani Mostafa, Khoshkenar Payam, Pothineni Venkata Raveendra, Kim Kwang Min, Murray Teresa A., Rajadas Jayakumar, Mills David K., Vashaee Daryoosh, Moharamzadeh Keyvan, Tayebi Lobat, From Solvent-Free Microspheres to Bioactive Gradient Scaffolds, *Nanomedicine: Nanotechnology, Biology, and Medicine* (2016), doi: 10.1016/j.nano.2016.10.008

From Solvent-Free Microspheres to Bioactive Gradient Scaffolds

Morteza Rasoulianboroujeni, MSc[a,b] , Mostafa Yazdimamaghani, MSc[b], Payam Khoshkenar, MSc[c,d],

Venkata Raveendra Pothineni, PhD[e], Kwang Min Kim, PhD[e], Teresa A. Murray, PhD[d], Jayakumar

Rajadas, PhD[e,f,g], David K. Mills, PhD[d], Daryoosh Vashaee, PhD[h], Keyvan Moharamzadeh, PhD[i],

Lobat Tayebi, PhD[a,b,j,*]

[a] Department of Developmental Sciences, Marquette University School of Dentistry, Milwaukee, WI 53233, USA

[b] Helmerich Advanced Technology Research Center, Oklahoma State University, Tulsa, OK 74106, USA

[c] The David H. Koch Institute for Integrative Cancer Research, Massachusetts Institute of Technology, Cambridge, MA 02139, USA

[d] Biomedical Engineering Department, Louisiana Tech University, Ruston, LA 71272, US

[e] Biomaterials and Advanced Drug Delivery Laboratory, Stanford University, Palo Alto, CA 94305, USA

[f] Department of Neurology and Neurological Sciences, Stanford University School of Medicine, Palo Alto, CA 94305, USA

[g] Stanford Cardiovascular Institute, Stanford University School of Medicine, Palo Alto, CA 94305, USA

[h] Electrical and Computer Engineering Department, North Carolina State University, Raleigh, NC 27606, USA

[i] School of Clinical Dentistry, University of Sheffield, Claremont Crescent, Sheffield, UK

[j] Department of Engineering Science, University of Oxford, Oxford OX1 3PJ, UK

Corresponding author at: Department of Developmental Sciences, Marquette University School of Dentistry, Milwaukee, WI 53233, USA. Email: lobat.tayebi@marquette.edu, lobat.tayebi@eng.ox.ac.uk

Word count for abstract: 147
Word count for complete manuscript: 5800
Number of figures/tables: 8/2
References: 59

Abstract

A solvent-free microsphere sintering technique was developed to fabricate scaffolds with pore size gradient for tissue engineering applications. Poly(D,L-Lactide) microspheres were fabricated through an emulsification method where TiO_2 nanoparticles were employed both as particulate emulsifier in the preparation procedure and as surface modification agent to improve bioactivity of the scaffolds. A fine-tunable pore size gradient was achieved with a pore volume of $30\pm2.6\%$. SEM, EDX, XRD and FTIR analyses all confirmed the formation of bone-like apatite at the 14th day of immersion in Simulated Body Fluid (SBF) implying the ability of our scaffolds to bond to living bone tissue. In vitro examination of the scaffolds showed progressive activity of the osteoblasts on the scaffold with evidence of increase in its mineral content. The bioactive scaffold developed in this study has the potential to be used as a suitable biomaterial for bone tissue engineering and hard tissue regeneration.

Keywords: Tissue engineering scaffold, pore size gradient, solvent-free method, microsphere sintering, mineralization, bone-like apatite

1. Background

Tissue engineering and regenerative medicine aim to create functional human tissue equivalents for organ repair and replacement through 3D scaffolds. [1] Pioneering studies have suggested that the micro-architecture of scaffolds might influence cell attachment and orientation and induce expression of different cellular behaviors. [2-4]

Many researchers have reported optimum pore size ranges necessary for different cell types or tissues. [5-7] Scaffolds with the optimum pore size range for each cell type provide an appropriate medium for cell growth since they establish a balance between the advantages and disadvantages of varying the scaffold's pore size. Pore size or porosity of the scaffold can affect nutrient supply, gas diffusion, metabolic waste removal, cell attachment and intracellular signaling [6-8]. Therefore, scaffolds that exhibit pore size covering different length scales may improve cellular activity; very small pores allow for molecule transport essential for any nutrition, waste removal and signaling; medium pores facilitate cell migration and capillary formation; and big pores help incorporation of nerves and blood vessels.[9] Thus, controlling pore size distribution through the scaffold may help researchers manage the cellular behavior more selectively.

Scaffolds with a gradient of pore size are the most popular example of such a distribution control representing advantages over uniform scaffolds for specific applications. A study by Sobral et al. showed that pore size gradient can improve cell seeding efficiency and induce a more homogenous distribution of cells within the scaffold. [10] They attributed the outcomes to the flow conditions throughout the scaffold during cell seeding. Pore size gradient also enables modulation of cell migration through the scaffold. The scaffold is permeable to cells from one side due to large pores and impermeable from the other side due to small pores. Such a design will facilitate the study of the direction of cell migration. Taking this strategy into account, Harley et al. produced collagen-based,

porous tubular scaffolds to facilitate the study of myofibroblast migration during peripheral nerve regeneration. [11]

Such a scaffold has the potential not only to become a powerful tool for basic studies on the effects of different pore sizes on cell behavior within identical microenvironments [12] but also in applications for targeting the formation of composite tissues (the epiphyseal growth plate), tissue interfaces (myotendinous junctions), and potential clinical use for guided tissue regeneration. Tissue interfaces are significant regions wherein tissue transition from one type into another occurs. Scaffolds with variation in pore size may provide an appropriate microenvironment for two or more cell types to grow concurrently. For instance, fabricating scaffolds with gradients in pore sizes allowing high vascularization and direct osteogenesis on one side of the scaffold, while promoting differentiation and osteochondral ossification on the other, is appealing in terms of reproducing multiple tissues and tissue interfaces on the same biomaterial scaffold. [13]

Different techniques have been employed to fabricate scaffolds with controlled pore size distribution including centrifugation method, rapid prototyping, spinning technique, salt leaching etc. [10-12, 14, 15] Among these methods, rapid prototyping represents excellent control over various scaffold parameters including architecture. However, clinical application of the method is limited due to high machine cost, design and fabrication time involved. Moreover, high processing temperatures in some rapid prototyping techniques limit their ability to process some polymers and biomolecules. [16] In addition, some of rapid prototyping techniques suffer from limited resolution, slow processing and the use of solvent. [17, 18] Therefore, the development of new fabrication methods wherein scaffold architecture can be controlled but eliminates the abovementioned drawbacks is highly desired.

The aim of this study was to develop a solvent-free microsphere sintering technique to produce scaffolds with pore size gradient for tissue engineering applications. This method enables high level

control over the pore size distribution through the scaffold. Although microsphere sintering has been employed to fabricate various 3D scaffolds, [19-25] creating solvent-free scaffolds with pore size gradient based on this method has not been previously reported. Our results demonstrate that using such a method, a perfect control over the scaffold architecture could be simply, reproducibly and cheaply achieved. The scaffolds seem to provide an excellent bioactive medium for calcium phosphate deposition, osteoblast attachment and biomineralization.

2. Methods

2.1. Materials

PDLA (100DL 7E, Inherent Viscosity: 0.6-0.8 dL/g, Mw 75000-120000 g/mol, cryo-milled powder) powder was purchased from Lakeshore Biomaterials (Birmingham, AL). Titanium Dioxide (21 nm primary particle size (TEM), 35-65 m^2/g surface area (BET)) was obtained from Sigma-Aldrich (St. Louis, MO). Mouse osteoblasts (7F2 CRL 12557) were obtained from American Type Culture Collection. Complete alpha MEM, Dulbecco's phosphate buffer (DPBS) and Pen-Strep solutions were purchased from GIBCO Inc. (Carlsbad, CA). Alizarin red and Von Kossa staining reagents were purchased from sigma Aldrich (St. Louis, MO). Fetal bovine serum and TryplE select cell dissociating solution were from Phenix (Asheville, NC) and Invitrogen (Carlsbad, CA), respectively. All other chemicals were of reagent grade.

2.2. Fabrication of microspheres

A solvent-free emulsification method was developed in our lab to fabricate PDLA microspheres coated with TiO_2 nanoparticles. Briefly, PDLA (250 mg) and TiO_2 nanoparticles (70 mg) were dispersed in pure water (50 ml) and bath-sonicated for 15 min in order to obtain a uniform dispersion. The dispersion was then heated to 80℃ while being stirred at 800 rpm for 2 hours followed by cooling at

4℃. Microspheres were then washed 3 times and collected using sieves of various mesh sizes (75, 150, 300 and 425µm) in order to remove residual TiO_2 nanoparticles and separate microspheres of the same size, respectively.

2.3. Fabrication of gradient scaffolds

Gradient scaffolds were fabricated through a modified microsphere sintering method. To create a pore size gradient, microspheres of each size range (75-150, 150-300 and 300-425 µm) were decanted into a mold layer by layer. The microspheres were then sintered at 90℃ for 45 min followed by cooling at room temperature. Homogenous scaffolds could also be prepared using microspheres of the same size range.

2.4. Morphology of microspheres and scaffolds

The morphology of microspheres and scaffolds was studied using Scanning Electron Microscopy (SEM) and micro computed tomography (micro-CT). Spherical shape of prepared microspheres, presence of TiO_2 nanoparticles on the surface of microspheres, interconnected porous structure and pore size gradient were expected to be verified by SEM and micro-CT.

For SEM, samples were placed on a bilateral tape and sputter-coated with gold using a SPI-Module Sputter Coater. Finally, samples were observed under a scanning electron microscope (Hitachi S-4800) using back-scattering and secondary electron modes at different magnifications.

The micro-CT system consisted of a Hamamatsu L9181-02 micro-focal X-ray source and a flat panel X-ray detector (Varian 2520DX). A micro-positioning stage between the source and detector allows specimens to be manipulated in space with four degrees of freedom. Micro-CT reconstruction was implemented using the Varian Cone-Bean CT reconstruction software. The CT scan consisted of 400 step and shoot projections with a circular trajectory. The images were acquired at 100 kV and 80

µA, with 0.5 second exposure per view angle. The images were reconstructed on to 25 micron × 25 micron × 25 micron voxels. ImageJ 1.5i software (National Institute of Health, USA) was used to analyze the micro-CT data. The binary images (Figure 3(D-F)) and pore outlines (Figure 3(G-I) of each cross-section of the scaffold were produced using the software for further analysis. Pore size distribution through the scaffold was determined using particle analyzer feature (see supplementary data). The connectivity of the pores was measured using BoneJ plugin. The image sequence was purified first and then Euler characteristic and connectivity density (number of trabeculae per unit volume) were calculated by means of the software.

2.5. Bioactivity of scaffolds

2.5.1. Mineralization in Simulated Body Fluid (SBF)

SBF was prepared according to the procedure described by Kokubo et al. [26] **Table 1** represents the nominal concentrations of different ions in the prepared SBF compared to human blood plasma. Bioactivity of scaffolds was evaluated through immersion in the prepared SBF solution at 37℃ for 14 days. At regular time intervals (1, 3, 7 and 14 days), samples were taken out, rinsed with distilled water and analyzed after drying. To determine apatite formation, Fourier Transform Infra-Red spectroscopy (FTIR), X-Ray Diffraction (XRD) (See supplementary data), Energy-dispersive X-ray spectroscopy (EDX) and SEM techniques were employed.

Functional groups of the scaffolds prior to immersion in SBF and newly formed ones during immersion were characterized by FTIR (Varian 680-IR spectrometer, Agilent Tech, USA). First, the dried scaffolds were grinded and mixed with KBr. The FTIR spectra were then collected at a spectrum resolution of 1 cm^{-1} over the measurement range from 4000 to 400 cm^{-1}.

SEM (Hitachi S-4800) and EDX (Evex) were used to observe the morphology and determine the chemical composition of the precipitated minerals on the scaffolds, respectively.

2.5.2. Biomineralization in mouse osteoblast culture

2.5.2.1. Cell culture and scaffold seeding

Mouse osteoblasts (7F2 CRL 12557) were cultured using standard aseptic cell culture techniques. The osteoblasts were maintained and passaged in complete alpha MEM containing alpha MEM, 10% (v/v) fetal bovine serum and 1% (v/v) Penicillin-Streptomycin (GIBCO). For passaging and transferring the osteoblasts onto the scaffolds, a 1% TryplE (GIBCO) select cell dissociating solution was used. Scaffolds were dipped in 90% (v/v) ethanol and dried under laminar airflow under aseptic conditions in a cell culture hood to prepare them for seeding. A cell suspension was prepared in sterile Dulbecco's Phosphate Buffered solution with a cell concentration of 2×10^6 cells per milliliter and was used to seed the scaffolds. The seeded scaffolds were then covered with complete alpha MEM growth medium and incubated at 37°C with 5% CO_2. For SEM imaging, the samples were fixed overnight in 2% Glutaraldehyde with 4% PFA (Paraformaldehyde) in 0.1 M Na Cacodylate Buffer (pH = 7.3) at 7th day of culture. Then, the scaffolds were washed twice for 5 min in the same buffer. Later, scaffolds were post-fixed for 1 hr in 1% aqueous Osmium Tetroxide (OSO_4). Then, the scaffolds were washed twice for 5 min with distilled H_2O and dehydrated in increasing ethanol series: 50-70-90-100-100% (v/v). They are subject to Critical Point Dry (CPD) with liquid CO_2 in Tousimis Autosamdri 814. The scaffolds were mounted with double-sided carbon tape on Al stubs. Finally, they were sputter-coated with Pd/Au - 100Å layer ~10 min with the Denton DeskII system.

2.5.2.2. Histology and staining techniques

Alizarin Red and Von Kossa histochemical staining was used to estimate the amount of calcium phosphate secreted by cells after attachment and differentiation. Scaffolds were first washed with sterile HBSS to remove any traces of serum and then fixed with 95% (v/v) ethanol on day 7, 14, and

21. Scaffolds were then flash frozen by immersion in liquid nitrogen and crushed using mortar and pestle to make a fine powder. The powder (5 mg) was then added to a 2 ml centrifuge tubes and stained with either Alizarin Red or Von Kossa for separate quantification of calcium and phosphate, respectively. For calcium quantification, Alizarin Red S aqueous solution (2% w/v, pH = 4.1 to 4.3) was added to the scaffolds powder and kept in room temperature for 5 min. Samples were de-stained by 7% (v/v) acetic acid for 15 minutes and centrifuged at 14000 rpm for 10 min, the supernatants were collected and analyzed by NANODROP 2000 in UV/Vis absorbance mode. For Von Kossa staining, 250 ul of 1% (w/v) silver nitrate aqueous solution was added to the crushed scaffolds, incubated under U.V light for 20 minutes and washed 5 times with distilled water. The samples were then incubated with 250 μl of 5% (w/v) sodium thiosulfate for 5 minutes to remove unreacted silver. Tubes were centrifuged at 14000 rpm for 10 min, the supernatants were collected and analyzed by NANODROP 2000 in UV/Vis absorbance mode.

3. Results

3.1. Morphology of microspheres and scaffolds

Morphology of the prepared microspheres could be observed in **Figure 1**. As seen in the figure, TiO_2 covers the surface of polymeric microspheres indicating successful physical surface modification. TiO_2 nanoparticles have been reported to increase wettability (hydrophilicity) and improve cell attachment when added to polyesters like PDLA. [19, 27] Furthermore, the spherical shape of the obtained particles (Figure 1(A, B)) together with the presence of TiO2 on the surface (Figure 1(C, D)) corresponds to the emulsifying properties of TiO_2 nanoparticles.

Figure 2 illustrates the morphology of the prepared scaffolds. The employed strategy to fabricate the scaffolds yielded an interconnected porous structure (Figure 2(A, B)); if a container is filled with

spheres, the empty spaces between them all are interconnected. The pore size gradient could be also observed in SEM images (Figure 2(C, D)).

Figure 3 represents the micro-CT images taken from different cross-sections of the scaffold. The scaffolds consist of three major regions; the first region (Figure 3(A)) made of microspheres of 75-150 µm exhibits very small pores; as the size of microspheres increases to 150-300 µm and 300-425 µm in the second (Figure 3(B)) and third (Figure 3(C)) regions, respectively, the pore size enlarges evidently. Figure 3(D-F) and Figure 3(G-I) show binary images and pore outlines produced by ImageJ software, respectively. Euler characteristic and connectivity density (Conn.D) were found to be -2033 and 18.7 mm^{-3}, respectively.

The micro-CT and SEM images confirmed the pore size gradient inside and on the surface of the scaffold as well as the interconnectivity of the pores.

3.2. Bioactivity of Scaffolds

3.2.1. Mineralization in SBF

SEM, EDX, FTIR and XRD (See supplementary data) analyses were used to study the morphology, composition and crystallinity of the mineral formed on the scaffolds after immersion in SBF for 1, 3, 7 and 14 days. **Figure 4** indicates the SEM images and EDX analysis of the samples before immersion in SBF and after certain immersion times. Before immersion, titanium was the major element detected by EDX implying the presence of TiO_2 on the surface of microspheres and scaffolds (Figure 4(A)). This finding perfectly matches with our observation in the SEM images of the prepared microspheres (Figure 1) and fully supports the emulsifying properties of TiO_2 nanoparticles in our system. A small amount of aluminum was also detected before immersion in SBF and few days after that which could be a result of using aluminum molds to heat the microspheres during the sintering stage. It could be

seen in the Figure 4(B) that only after 1 day calcium ions as well as chloride ions start to be adsorbed on the surface. Interestingly, no phosphorous was detected after the first day of immersion and this element representing phosphate ions appeared on the 3rd day of immersion. Precipitation of these minerals could be obviously seen in the corresponding SEM image. Sodium ions were also deposited along with phosphate ions on the 3rd day. Afterwards, calcium and phosphate ions concentrated on the surface to the extent that no other ions except them were detected on the 14th day. SEM images apparently illustrate the precipitation progress of calcium phosphate minerals so that the scaffolds' pores were completely filled on the 14th day of immersion. Calculating the Ca/P ratio of the precipitated calcium phosphate (**Table 2**) in the last day of immersion as well as the 7th day leads to a quite interesting data:

(Ca/P) ratio at 14th day = (AT% for Ca)/(AT% for P) = 62.41/37.59 $\simeq$ 1.66

(Ca/P) ratio at 7th day = (AT% for Ca)/(AT% for P) = 54.26/25.71 $\simeq$ 2.11

where AT% is the molar fraction of each element in the compound and could be obtained from EDX data (Table 2).

The Ca/P ratio at the last day of immersion found to be around 1.66 which is close to that of hydroxyapatite (HA) [28] and the mineral could be theoretically considered as calcium deficient HA. However, the EDX analysis results alone cannot be exploited to unequivocally determine the nature of the calcium phosphate. Occlusion of $CaCl_2$ [29] along with the incorporation of calcium into the calcium titanate ($CaTiO_3$) which will be discussed in detail could account for the high Ca/P ratio at 7th day.

The FTIR spectra of immersed scaffolds for different time intervals in the SBF showed establishment of additional peaks associated to the formed calcium phosphate layer on the surface of the scaffolds

(**Figure 5**). Appearance of peaks at 1032 cm^{-1} raised from v_3 PO$_4$ vibrations (P-O stretching mode) and at 602 cm^{-1} and 565 cm^{-1} pertaining to v_4 PO$_4$ vibrations (O-P-O bending mode) [30] confirms the formation of calcium phosphate layer. Besides, although the v_1 PO$_4$ band (P-O stretching) at 960 cm^{-1} is only of minor intensity in IR spectroscopy, its presence is also of interest since it is indeed observed at this position in apatite phases or OCP. Furthermore, the band at 878 cm^{-1} could be attributed to the P-OH stretching of HPO$_4^-$ bearing apatite. [31] It has been reported that two distinct band at 1195 and 916 cm^{-1} which are assignable to HPO$_4^{2-}$ are detectable for OCP but not for apatite. [31] The small peak detected in the spectrum of the 3rd day of immersion at 1260 cm^{-1} could be barely assigned to this functional group indicating the presence of OCP. Interestingly, the peak disappeared in the following days implying the presence of apatite as the main phase of the precipitated mineral.

Taking a closer look at the FTIR spectra of the samples, the poorly crystalline structure of the formed layer could be also confirmed by the small splitting of degenerate modes. In complex crystalline phosphates, local crystal field effects may lower the symmetry of the tetrahedral PO$_4^{3-}$ ion. This results in the splitting of degenerate modes and also in the occasional appearance of infra-red forbidden frequencies. [30] In this case, the splitting of the P-O anti-symmetric bending mode at 550-600 cm^{-1} and degenerate phosphate stretching mode (1000-1100 cm^{-1}) increases as the percent crystallinity increases. [29] This is in agreement with XRD results revealing that the precipitated minerals are poorly crystalline (See supplementary data).

To further investigate the morphology of the precipitated mineral, high magnification SEM images were employed. **Figure 6** shows the morphology of the precipitated mineral at the 7th day of immersion. As could be seen in the figure, the precipitated layer was up to 10 µm thick only after 7 days of immersion (Figure 6(A, B)). It seems that the precipitated layer consists of numerous hemispherical particles of 2-5 µm in diameter grown on the surface (Figure 6(C)). These particles are

likely to be the nucleation sites of calcium phosphate precipitate (Figure 6(D)). The cracks observed in the precipitate layer might be a result of desiccation of the samples before imaging, generating a contracting force.

3.2.2. Biomineralization in osteoblast culture

It has been shown that presence of calcium and phosphate promotes the osteoconductivity of scaffolds. [32] These inorganic components of hydroxyapatite [$Ca_{10}(PO_4)_6(OH)_2$] trigger upcoming scaffold mineralization, leading to formation of bone-like structure. Calcium and phosphate rich microenvironment of scaffolds enhances the osteocytic phenotype of bone-producing cells, i.e., osteoblasts. Calcium content of mineralized scaffolds was quantitatively determined using Alizarin red staining. As can be seen in **Figure 7**(A), time-dependent deposition of calcium on scaffolds has increased over 21 days.

Presence of phosphate in the calcium phosphate phase of mineralized scaffolds was quantified by Von-Kossa staining. Anionic part of phosphates in calcium phosphate mineralized matrix is stained by Von Kossa. As can be seen in Figure 7(A), enhancement of mineral matrix deposition on the scaffolds is evident over 21 days. Von Kossa staining indicates both the amount of phosphate containing minerals and amount of organic phase of matrix. Therefore, the more staining intensity, the more amounts both organic and inorganic matrix. At 7th day, the seeded scaffolds showed more calcium content than phosphate. This is in agreement with the results of mineralization in SBF that calcium deposition occurs before phosphate deposition. Interestingly, the phosphate content of scaffolds increased over five folds at 21st day of culture.

Figure 7(B-G) demonstrates the SEM images of osteoblasts cultured on the scaffolds. The osteoblasts grew within the pores of the scaffold with their multiple cell processes branching from one microsphere

to another forming an adherent plexus all over the scaffold microspheres. It can be vividly seen that osteoblasts have attempted to anchor their cytoskeletal projections (lamellipodia and Filopodia) between the microspheres revealing the bioactive characteristics of the scaffolds to induce cell migration along and in depth of the substrates. As shown in Figure 7(B, C), osteoblasts have covered the surface of the microspheres indicating bioactive topography of the microspheres. Also, in Figure 7(D, E), we can see cells grown on the adjoining areas (bonding points) of the microspheres suggesting the optimum porous structure of the scaffolds to promote the cell propagations between the microspheres. Interestingly, the secreted minerals by the cells could be easily detected in the SEM images (e.g. Figure 7(F)) which supports the biomineralization capability of the scaffold. Figure 7(G) shows the cells anchored to the microspheres beneath the surface which demonstrates the ability of the cells to penetrate into the scaffold's bulk. A penetration depth of at least 885 µm is suggested based on preliminary multiphoton microscopy studies (data not shown) which could be a promising sign of using these scaffolds as potential substrates for 3D culture and joint tissue engineering.

4. Discussion

The emulsifying properties of TiO_2 nanoparticles could be attributed to the relatively weak interaction (hydrogen bond) between the brønsted acid site (Ti-OH) of TiO_2 and polar groups of PDLA like C=O. [33] Heating PDLA above its glass transition temperature, the polymer softens and a polymer-in-water emulsion is obtained. It is assumed that TiO_2 nanoparticles are adsorbed at the polymer-water interface to stabilize polymer-in-water emulsion by reducing interfacial tension. The mechanism has been schematically represented in **Figure 8**. We exploited this mechanism to obtain solvent-free microspheres coated with TiO_2 nanoparticles.

According to Hildebrand and coworkers [34], for TiO_2 nanoparticles to sit on the interface of polymer-water, they have to be wetted by both polymer and water. The assembly of the particles onto the

interface helps the interface bend in the direction of the more poorly wetting phase (i.e. the polymer) and consequently facilitates its emulsification into droplets. The adhesion energy of the TiO_2 particles at the interface could be described by the following equation:

$$\Delta E = \pi R^2 \sigma (1 - |\cos\theta|)^2 \quad \text{Equation 1}$$

where ΔE is the escape energy needed to remove the particle from the interface, R is the radius of the particle, σ is the interfacial tension between two phases and θ is the contact angle between the TiO_2 nanoparticle and the polymer.

According to the equation, decreasing the particle size decreases the adhesion energy. However, one should note that the particle size may also affect the contact angle. Smaller particles represent higher surface area and more active functional groups on the surface which may cause a better interaction with the polymer droplet surface. This may result in contact angles closer to 90° and enhanced adhesion energy.

Heating the microspheres above the glass transition of PDLA results in enhanced molecular movement and increases the opportunity for diffusional rearrangement of polymer chain segments. Increasing chain motility, new entanglements may form between the surface chains of two adjacent microspheres leading to a united porous architecture after cooling. We obtained scaffold with porosities in the range of 30±2.6% (See supplementary data for details about porosity) through this method. Sintering temperature and sintering time are the most important processing parameters which affect scaffold properties including pore size and porosity. Elevated sintering temperature and longer sintering time are expected to have the same effects since both of them increase the extent of microsphere fusion. Jiang et al. found that a higher sintering temperature as well as a longer sintering time results in a

greater median pore size but decreased pore volume. [21] Their finding might be a result of possible closure of pores among the microspheres which occurs for the smaller pores first.

The highly active surface of our samples for calcium phosphate nucleation and growth may be a result of surface modification by TiO_2 nanoparticles and the mechanism by which it happens is of our great interest. Gerhardt et al. found non-stoichiometric HA crystals on both pure PDLA and PDLA/TiO_2 composite films after immersion in supersaturated SBF. Based on their observation two possible mechanisms could be proposed for apatite formation from the SBF solution: [35]

1- PDLA surface: PDLA surface is hydrolyzed when gets into contact with water converting ester linkages into surface carboxylic groups (COOH). COOH groups dissociate into carboxylate anions (COO$^-$) providing a negatively charged surface for binding of calcium ions (Ca^{2+}). As a result, nucleation and subsequent HA crystal growth is stimulated.

2- TiO_2 nanoparticles: presence of TiO_2 nanoparticles causes water absorption on the surface of microspheres. As a result, titanium hydroxide (Ti-OH) groups form. Dissociation of these Ti-OH groups leads to a negatively charged surface providing sites for calcium phosphate nucleation.

Both of the mechanisms suggest the formation of a negatively charged surface group which has been reported to be effective for apatite nucleation while positively charged surface groups are claimed to have weaker apatite nucleating ability. [36] However, incorporation of TiO_2 nanoparticles improved the bioactivity of PDLA films [35] indicating the key role of these nanoparticles in bioactivity. Furthermore, in our study the surface of the microspheres responsible for interaction with SBF solution ions was mainly covered by TiO_2 nanoparticles (Figure 1). Therefore, the second mechanism seems to be the dominant mechanism of bioactivity and should be considered in detail. TiO_2 nanoparticles have several acid sites including Lewis acid site (Ti$^+$) and Brønsted acid site (Ti-OH) on the surface. [37, 38]

X-ray Absorption Fine Structure (XAFS) measurements at the Ti K-edge performed by Chen et al. showed shorter Ti-O distances for surface TiO_2 resulting from Ti-OH bonding on the surface of nanoparticles. [39] These Ti-OH groups could be assumed to trigger the nucleation in the apatite formation process. It has been suggested that Ti-OH groups incorporate the calcium ions in the SBF solution to form calcium titanate. As the Ca^{2+} cations accumulate, the consequent positively charged surface incorporate the phosphate ions in the solution to form an amorphous calcium phosphate (ACP) which later crystallize into bonelike apatite. [40] The formation of the calcium titanate is assumed to be initiated by electrostatic interaction of negatively charged units of titania dissociated from the Ti-OH groups with the positively charged calcium ions in the solution. Our finding that calcium deposition occurs before phosphate deposition is perfectly in agreement with the suggested mechanism. Gemelli et al. achieved the same outcome about the deposition order when soaked treated titanium in supersaturated S-SBF solution. They also detected calcium and titanium but no phosphorous at the interface between the titanium implant and bone indicating the ability of calcium titanate to link directly to the bone. [41] According to our EDX analysis, at the 1st day of immersion, only Ca^{2+} and Cl^- ions deposited from the solution and no phosphorous was detected until the 3rd day of immersion neither through EDX analysis nor FTIR spectra. Titanium was the other element detected which could be assumed to exist both as the surface TiO_2 and incorporated into $CaTiO_3$. Adsorption of chloride anions instead of phosphate ones in the beginning stage of immersion could be attributed to the following facts:

1- Phosphate anions cannot effectively compete with chloride adsorption because of their relatively low charge density. [42]

2- Chloride anions have relatively high concentration in the prepared SBF solution compared to other anions (see Table 1) leading to enhanced adsorption of these ions. According to Langmuir adsorption isotherm, the extent of adsorption of a component depends on its concentration as follows:

$$n = \frac{MkC}{1+kC}$$ Equation 2   [43]

where, k and M indicate the affinity of the adsorbate for the adsorbent and the total capacity of the adsorbent, respectively; n represents the quantity of adsorbate sorbed per unit mass of sorbent and C is the equilibrium concentration of the adsorbate in the liquid phase.

Furthermore, competitive adsorption equations in a multi-component system could be derived from Langmuir isotherm as:

$$n_1 = \frac{Mk_1C_1}{1+k_1C_1+k_2C_2}$$ Equation 3   [44]

which indicates the importance of both concentration and affinity of the adsorbate.

Both EDX analysis and FTIR spectra confirm the adsorption of phosphate groups at the 3rd day of immersion. In this stage, the positive charge of the formed calcium titanate has been proposed to encourage interaction with the negatively charged phosphate groups in the solution to form amorphous calcium phosphate. [40] It should be noted that Na^+ cations were also adsorbed in this stage together with phosphate anions which could be also a result of high concentration of sodium ions in the solution compared to other cations (see Table 1). Furthermore, a kinetic and thermodynamic study by Rabadjieva et al. showed that the precipitated ACP from SBF solutions always contained impurities due to co-precipitation, ion substitution and incorporation phenomena. [45] We were unable to detect the expected ACP phase neither in XRD patterns (See supplementary data) nor FTIR spectra maybe because the ACP precipitate is a highly unstable phase and hydrolyzes almost instantaneously to more

stable phases. [46] The hydrolysis of pure ACP to apatite at the physiological pH of 7.4 and 37℃ has been reported to occur within 6 minutes. [47] As mentioned before, the ACP phase is expected to crystallize into bonelike apatite. HA has been reported to form through nucleation and growth directly from ACP [48, 49] or transformation of OCP. [42] We found some signs of presence of OCP at the 3rd day of immersion (after phosphate adsorption) in FTIR spectrum of the precipitated mineral. The small FTIR peak at 1260 cm^{-1} barely assigned to HPO_4^{2-} of OCP detected at the 3rd day of immersion could possibly support the formation of this compound as the precursor for HA particularly when the peak disappeared at the 7th day. It is in agreement with the fact that while HA is more stable thermodynamically, OCP formation is more favorable kinetically. [50, 51] However, further investigation is required to precisely determine if HA nucleates directly from ACP or forms through OCP dissolution-precipitation in such a system. In fact, the partial structural resemblances of poorly crystalline HA and OCP may result in relative similarity of experimentally obtained data. In the case of XRD patterns, the OCP peak at very low 2θ angles (around 4.7˚) may assist for confident distinguishing of two phases. However, low ranges are not always examined (just like this study) because of the specific diffractometer setup required. [31]

The hemispherical morphology of precipitates (Figure 6) on Ti-based surfaces has been previously observed in several studies and seems to be likely for both HA and OCP. [52, 53] It is worth mentioning that the precipitation of each phase highly depends on the composition of the SBF used. For instance, Lu et al. used R-SBF with the same HCO_3^- concentration level as in human blood plasma and found continuously growing crystals of OCP on the titanium surfaces with no transformation into apatite [52] while employing SBF solutions with lower HCO_3^- content (like the SBF used in this study) resulted in apatite formation on the surface of treated titanium alloys. [53]

Osteoblast culture showed time-dependent deposition of calcium and phosphate on scaffolds over a 21 days period. Negatively charged surface of scaffolds due to the presence of Ti-OH as well as

carboxylate anions (COO⁻) dissociated from carboxylic groups of PDLA triggered and promoted the deposition of calcium cations and subsequently absorption of phosphate anions. Due to the equilibrium complexation of anions and cations, adsorption of Ca^{2+} is dependent on PO_4^{3-} adsorption and vice versa. Therefore, initial calcium accumulation on the scaffolds, triggered the phosphate anions to precipitate. This can be seen in the phosphate content of scaffolds after 21 days which has been increased over five folds in comparison with 7th day.

Taking the both staining and previous characterization results into account, we came to the conclusion that osteoconductive pathway was progressed on the scaffolds in three phases: cell proliferation, ECM secretion, and finally mineralization. Co-localization of calcium and phosphate ions may be inferred from complex interaction between calcium and phosphate ions. It has been revealed that attached cells to the bioactive scaffolds, show more mineralized matrix than non-attached cells. [54] Cell adhesion is associated with protein binding on mineralized surface of the scaffolds. Therefore, calcium and phosphate secretion may suggest the expression of osteopontin, a phosphoprotein having calcium binding domains and is responsible for cell attachment and proliferation. Vitronectin is another protein associated with cell adhesion. Conformational changes on vitronectin occur upon its binding on the bioactive surfaces exposing more cell binding domains. [55-58] Highly porous and bioactive surface of the scaffolds enhanced protein binding on the calcium phosphate-rich surfaces. Choi et. al. [59] probed the effect of coating morphology and surface roughness on cell attachment and subsequent cellular response. Interestingly, they reported that spherulitic micro-morphology of mineralized coating, exhibited higher cell attachment compared to that plate-like and net-like micro-morphology. This may be attributed to the increased protein absorption on the spherulitic micro-morphology. As a comparison with their results, we can see in Figure 6 that the surface micro-morphology of our scaffolds, looks like nearly spherulitic rather than plate-like and net-like pattern. Hence, spherulitic micro-pattern of our scaffold surface coating presents a valuable surface morphology for cell expansion and adhesion.

References

1. Langer, R. and J.P. Vacanti, *Tissue engineering.* Science, 1993. **260**(2): p. 920-941.
2. Flemming, R., et al., *Effects of synthetic micro-and nano-structured surfaces on cell behavior.* Biomaterials, 1999. **20**(6): p. 573-588.
3. Desai, T.A., *Micro-and nanoscale structures for tissue engineering constructs.* Medical Engineering & Physics, 2000. **22**(9): p. 595-606.
4. Andersson, H. and A. Van Den Berg, *Microfabrication and microfluidics for tissue engineering: state of the art and future opportunities.* Lab Chip, 2004. **4**(2): p. 98-103.
5. Whang, K., et al., *Engineering bone regeneration with bioabsorbable scaffolds with novel microarchitecture.* Tissue engineering, 1999. **5**(1): p. 35-51.
6. Yang, S., et al., *The design of scaffolds for use in tissue engineering. Part I. Traditional factors.* Tissue engineering, 2001. **7**(6): p. 679-689.
7. Zeltinger, J., et al., *Effect of pore size and void fraction on cellular adhesion, proliferation, and matrix deposition.* Tissue Engineering, 2001. **7**(5): p. 557-572.
8. Van Tienen, T.G., et al., *Tissue ingrowth and degradation of two biodegradable porous polymers with different porosities and pore sizes.* Biomaterials, 2002. **23**(8): p. 1731-1738.
9. Fierz, F.C., et al., *The morphology of anisotropic 3D-printed hydroxyapatite scaffolds.* Biomaterials, 2008. **29**(28): p. 3799-3806.
10. Sobral, J.M., et al., *Three-dimensional plotted scaffolds with controlled pore size gradients: effect of scaffold geometry on mechanical performance and cell seeding efficiency.* Acta Biomaterialia, 2011. **7**(3): p. 1009-1018.
11. Harley, B.A., et al., *Fabricating tubular scaffolds with a radial pore size gradient by a spinning technique.* Biomaterials, 2006. **27**(6): p. 866-874.
12. Oh, S.H., et al., *In vitro and in vivo characteristics of PCL scaffolds with pore size gradient fabricated by a centrifugation method.* Biomaterials, 2007. **28**(9): p. 1664-1671.
13. Karageorgiou, V. and D. Kaplan, *Porosity of 3D biomaterial scaffolds and osteogenesis.* Biomaterials, 2005. **26**(27): p. 5474-5491.
14. Tamayo, A., et al., *Gradient pore size distributions in porous silicon oxycarbide materials.* Journal of the European Ceramic Society, 2008. **28**(9): p. 1871-1879.
15. Wu, H., et al., *Fabrication of chitosan-< i> g</i>-polycaprolactone copolymer scaffolds with gradient porous microstructures.* Materials Letters, 2008. **62**(17): p. 2733-2736.
16. Abdelaal, O.A. and S.M. Darwish, *Review of rapid prototyping techniques for tissue engineering scaffolds fabrication*, in *Characterization and Development of Biosystems and Biomaterials*. 2013, Springer. p. 33-54.
17. Peltola, S.M., et al., *A review of rapid prototyping techniques for tissue engineering purposes.* Annals of medicine, 2008. **40**(4): p. 268-280.
18. Yeong, W.-Y., et al., *Rapid prototyping in tissue engineering: challenges and potential.* Trends in biotechnology, 2004. **22**(12): p. 643-652.
19. Wang, Y., et al., *Poly (lactide-co-glycolide)/titania composite microsphere-sintered scaffolds for bone tissue engineering applications.* Journal of Biomedical Materials Research Part B: Applied Biomaterials, 2010. **93**(1): p. 84-92.
20. Singh, M., et al., *Microsphere-based scaffolds for cartilage tissue engineering: Using subcritical CO< sub> 2</sub> as a sintering agent.* Acta biomaterialia, 2010. **6**(1): p. 137-143.
21. Jiang, T., W.I. Abdel-Fattah, and C.T. Laurencin, *In vitro evaluation of chitosan/poly (lactic acid-glycolic acid) sintered microsphere scaffolds for bone tissue engineering.* Biomaterials, 2006. **27**(28): p. 4894-4903.
22. Wang, Y., et al., *Porous poly (lactic-co-glycolide) microsphere sintered scaffolds for tissue repair applications.* Materials Science and Engineering: C, 2009. **29**(8): p. 2502-2507.

23. Hu, X., et al., *Modified composite microspheres of hydroxyapatite and poly (lactide-co-glycolide) as an injectable scaffold.* Applied Surface Science, 2013.

24. Borden, M., M. Attawia, and C.T. Laurencin, *The sintered microsphere matrix for bone tissue engineering: in vitro osteoconductivity studies.* Journal of biomedical materials research, 2002. **61**(3): p. 421-429.

25. Wang, Y., et al., *In vitro osteogenesis of synovium mesenchymal cells induced by controlled release of alendronate and dexamethasone from a sintered microspherical scaffold.* Journal of Biomaterials Science, Polymer Edition, 2010. **21**(8-9): p. 1227-1238.

26. Kokubo, T. and H. Takadama, *How useful is SBF in predicting in vivo bone bioactivity?* Biomaterials, 2006. **27**(15): p. 2907-2915.

27. Liu, H., E.B. Slamovich, and T.J. Webster, *Increased osteoblast functions on nanophase titania dispersed in poly-lactic-co-glycolic acid composites.* Nanotechnology, 2005. **16**(7): p. S601.

28. Berzina-Cimdina, L. and N. Borodajenko, *Research of calcium phosphates using Fourier transform infrared spectroscopy.* Infrared spectroscopy–materials science. Engineering and Technology. InTech China, Shanghai, 2012: p. 123-148.

29. Blumenthal, N., A. Posner, and J. Holmes, *Effect of preparation conditions on the properties and transformation of amorphous calcium phosphate.* Materials Research Bulletin, 1972. **7**(11): p. 1181-1189.

30. Baddiel, C. and E. Berry, *Spectra structure correlations in hydroxy and fluorapatite.* Spectrochimica Acta, 1966. **22**(8): p. 1407-1416.

31. Drouet, C., *Apatite formation: why it may not work as planned, and how to conclusively identify apatite compounds.* BioMed research international, 2013. **2013**.

32. Dorozhkin, S.V., *Calcium orthophosphates: occurrence, properties, biomineralization, pathological calcification and biomimetic applications.* Biomatter, 2011. **1**(2): p. 121-164.

33. Nakayama, N. and T. Hayashi, *Preparation and characterization of poly (l-lactic acid)/TiO< sub> 2</sub> nanoparticle nanocomposite films with high transparency and efficient photodegradability.* Polymer degradation and stability, 2007. **92**(7): p. 1255-1264.

34. Finkle, P., H.D. Draper, and J.H. Hildebrand, *The theory of emulsification1.* Journal of the American Chemical Society, 1923. **45**(12): p. 2780-2788.

35. Gerhardt, L.-C., G. Jell, and A. Boccaccini, *Titanium dioxide (TiO2) nanoparticles filled poly (D, L lactid acid)(PDLLA) matrix composites for bone tissue engineering.* Journal of Materials Science: Materials in Medicine, 2007. **18**(7): p. 1287-1298.

36. Tanahashi, M. and T. Matsuda, *Surface functional group dependence on apatite formation on self-assembled monolayers in a simulated body fluid.* Journal of biomedical materials research, 1997. **34**(3): p. 305-315.

37. Nakayama, N. and T. Hayashi, *Preparation of TiO< sub> 2</sub> nanoparticles surface-modified by both carboxylic acid and amine: Dispersibility and stabilization in organic solvents.* Colloids and Surfaces A: Physicochemical and Engineering Aspects, 2008. **317**(1): p. 543-550.

38. Chen, X., *Preparation and property of TiO 2 nanoparticle dispersed polyvinyl alcohol composite materials.* Journal of materials science letters, 2002. **21**(21): p. 1637-1639.

39. Chen, L.X., et al., *XAFS studies of surface structures of TiO2 nanoparticles and photocatalytic reduction of metal ions.* The Journal of Physical Chemistry B, 1997. **101**(50): p. 10688-10697.

40. Takadama, H., et al., *XPS study of the process of apatite formation on bioactive Ti–6Al–4V alloy in simulated body fluid.* Science and Technology of Advanced Materials, 2001. **2**(2): p. 389-396.

41. Gemelli, E., C.X. Resende, and G.D. de Almeida Soares, *Nucleation and growth of octacalcium phosphate on treated titanium by immersion in a simplified simulated body fluid.* Journal of Materials Science: Materials in Medicine, 2010. **21**(7): p. 2035-2047.

42. Xie, Y., et al., *Nucleation and growth of calcium–phosphate on Ca-implanted titanium surface.* Surface science, 2006. **600**(3): p. 651-656.

43.   Langmuir, I., *The adsorption of gases on plane surfaces of glass, mica and platinum.* Journal of the American Chemical society, 1918. **40**(9): p. 1361-1403.

44.   Harter, R.D. and D.E. Baker, *Applications and misapplications of the Langmuir equation to soil adsorption phenomena.* Soil Science Society of America Journal, 1977. **41**(6): p. 1077-1080.

45.   Rabadjieva, D., et al., *Biomimetic transformations of amorphous calcium phosphate: kinetic and thermodynamic studies.* Journal of Materials Science: Materials in Medicine, 2010. **21**(9): p. 2501-2509.

46.   Boskey, A. and A. Posner, *Magnesium stabilization of amorphous calcium phosphate: a kinetic study.* Materials Research Bulletin, 1974. **9**(7): p. 907-916.

47.   Eanes, E.D., *Amorphous calcium phosphate: thermodynamic and kinetic considerations*, in *Calcium phosphates in biological and industrial systems*. 1998, Springer. p. 21-39.

48.   Kokubo, T., T. Matsushita, and H. Takadama, *Titania-based bioactive materials.* Journal of the European Ceramic Society, 2007. **27**(2): p. 1553-1558.

49.   Jonášová, L., et al., *Biomimetic apatite formation on chemically treated titanium.* Biomaterials, 2004. **25**(7): p. 1187-1194.

50.   Heughebaert, J. and G. Nancollas, *Kinetics of crystallization of octacalcium phosphate.* The Journal of Physical Chemistry, 1984. **88**(12): p. 2478-2481.

51.   Barrere, F., et al., *Biomimetic coatings on titanium: a crystal growth study of octacalcium phosphate.* Journal of Materials Science: Materials in Medicine, 2001. **12**(6): p. 529-534.

52.   Lu, X. and Y. Leng, *TEM study of calcium phosphate precipitation on bioactive titanium surfaces.* Biomaterials, 2004. **25**(10): p. 1779-1786.

53.   Lee, B.H., et al., *Surface modification by alkali and heat treatments in titanium alloys.* Journal of biomedical materials research, 2002. **61**(3): p. 466-473.

54.   Silva, S., et al., *Effect of biphasic calcium phosphate on human macrophage functions in vitro.* Journal of Biomedical Materials Research Part A, 2003. **65**(4): p. 475-481.

55.   Palin, E., H. Liu, and T.J. Webster, *Mimicking the nanofeatures of bone increases bone-forming cell adhesion and proliferation.* Nanotechnology, 2005. **16**(9): p. 1828.

56.   Webster, T.J. and J.U. Ejiofor, *Increased osteoblast adhesion on nanophase metals: Ti, Ti6Al4V, and CoCrMo.* Biomaterials, 2004. **25**(19): p. 4731-4739.

57.   Webster, T.J., et al., *Mechanisms of enhanced osteoblast adhesion on nanophase alumina involve vitronectin.* Tissue engineering, 2001. **7**(3): p. 291-301.

58.   Webster, T.J., R.W. Siegel, and R. Bizios, *Osteoblast adhesion on nanophase ceramics.* Biomaterials, 1999. **20**(13): p. 1221-1227.

59.   Choi, S. and W.L. Murphy, *The effect of mineral coating morphology on mesenchymal stem cell attachment and expansion.* Journal of materials chemistry, 2012. **22**(48): p. 25288-25295.

Table 1 Nominal concentrations of ions in the prepared SBF compared to human blood plasma

Ion	Ion concentration (mM)	
	Blood Plasma	SBF
Na^+	142.0	142.0
K^+	5.0	5.0
Mg^{2+}	1.5	1.5
Ca^{2+}	2.5	2.5
Cl^-	103.0	147.8
HCO_3^-	27.0	4.2
HPO_4^{2-}	1.0	1.0
SO_4^{2-}	0.5	0.5
pH	7.2-7.4	7.4

Table 2 Composition of the mineral precipated on the scaffold after immersion in SBF for 1, 3, 7, 14

days obtained by EDX analysis

Elements	AT % (Molar Fraction)				
	Before Immersion	1st Day	3rd Day	7th Day	14th Day
Ti (K)	77.84	42.96	19.25	13.82	-
Cl (K)	-	8.57	35.8	6.21	-
Na (K)	-	-	23.11	-	-
Ca (K)	-	3.72	7.39	54.26	62.41
P (K)	-	-	5.29	25.71	37.59
Other (Al, …)	22.16	44.75	9.16	-	-

Figure 1 SEM images of prepared microspheres: the spherical shape (A, B) and the presence of TiO_2 on the surface (C, D) can be easily seen.

Figure 2 SEM images of interconnected porous structure (A, B) and pore size gradient (C, D) of the prepared scaffolds

Figure 3 Micro-CT images of different cross-sections of the scaffold with small (microspheres of 75-150 µm) (A), average (microspheres of 150-300 µm) (B) or big (microspheres of 300-425 µm) (C) pore size. Binary images (D-F) and pore outlines (G-I) has been produced using ImageJ software. The pore size gradient can be seen from top to bottom.

Figure 4 SEM images and EDX analysis of the scaffolds before (A) and after immersion in SBF for 1 (B), 3 (C), 7 (D) and 14 (E) days

Figure 5 FTIR spectra of the samples before (A) and after immersion in SBF for 1 (B), 3 (C), 7 (D) and 14 (E) days.

Figure 6 SEM micrographs of the precipitated mineral on the scaffolds after 7 days of immersion in SBF: Thickness of up to 10 µm (A, B), hemispherical particles of 2-5 µm in diameter grown on the surface (C) and possible nucleation sites of calcium phosphate precipitate (D) could be seen

Figure 7 Quantitative demonstration of calcium (dark pattern) and phosphate (light pattern) biomineralization (A) along with SEM images of osteoblasts covering the surface of the scaffolds (B, C); anchoring projections between microspheres (D, E); secreting minerals (F); penetrating in depth of the scaffold (G)

Figure 8 Schematic representation of PDLA-water emulsification through TiO$_2$ nanoparticles
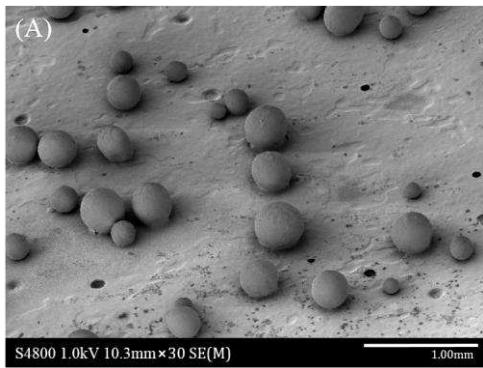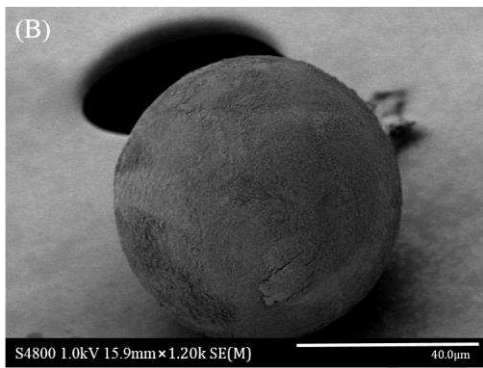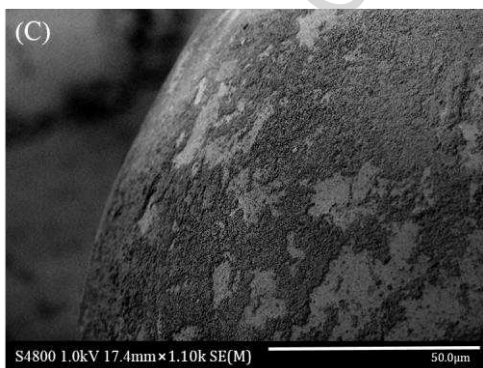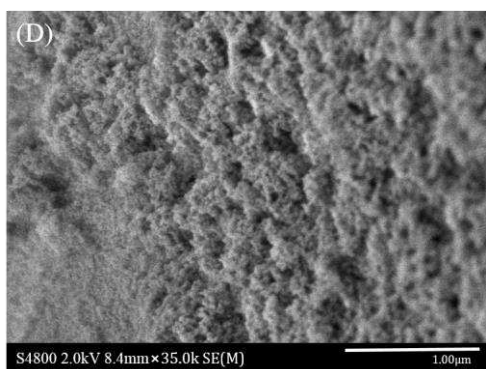
Fig. 1A

Fig. 1B

Fig. 1C

(D)

S4800 2.0kV 8.4mm×35.0k SE(M)   1.00μm

Fig. 1D
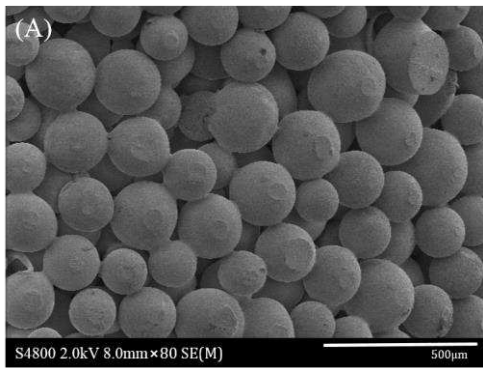
Fig. 2A

Fig. 2B
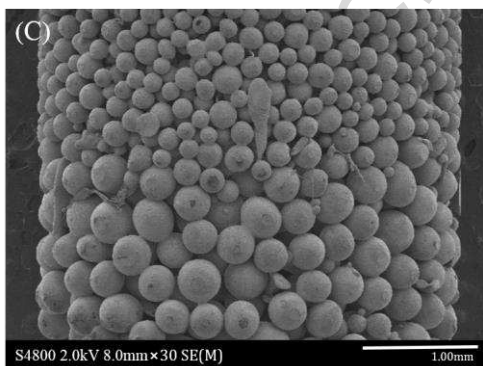
Fig. 2C
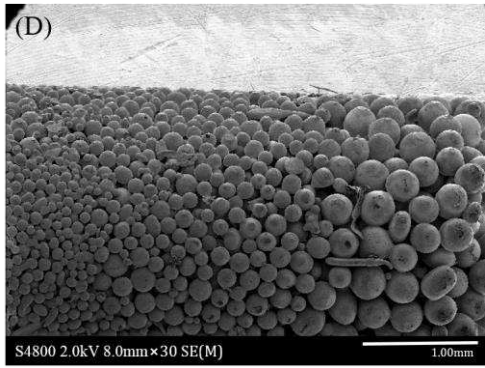
Fig. 2D
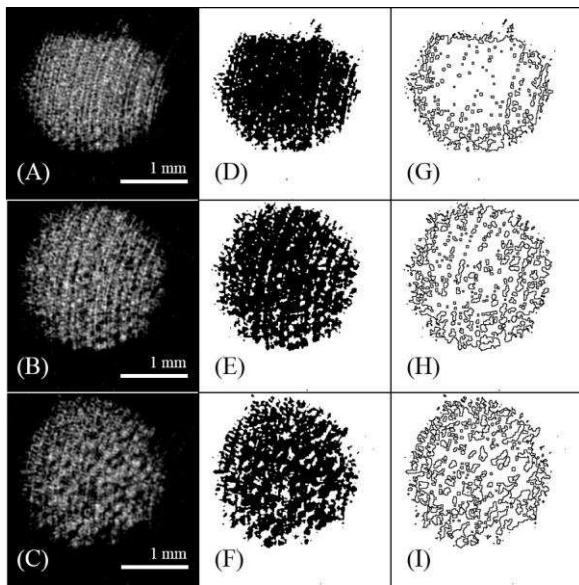
Fig. 3
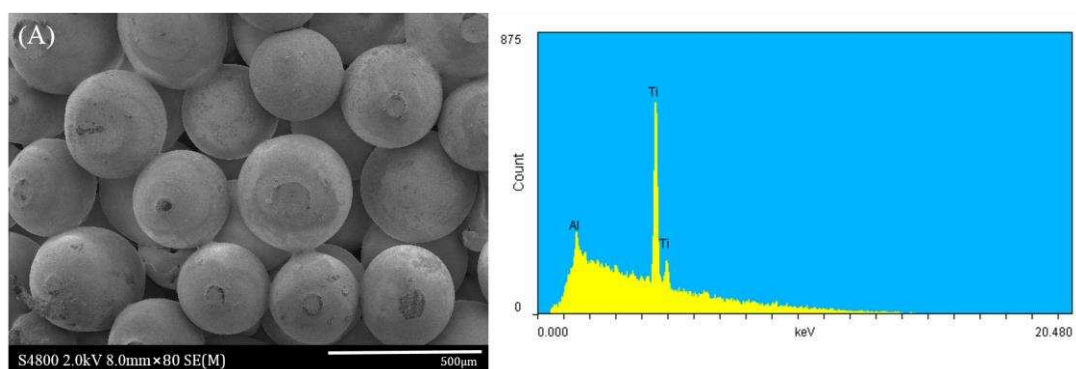
Fig. 4A
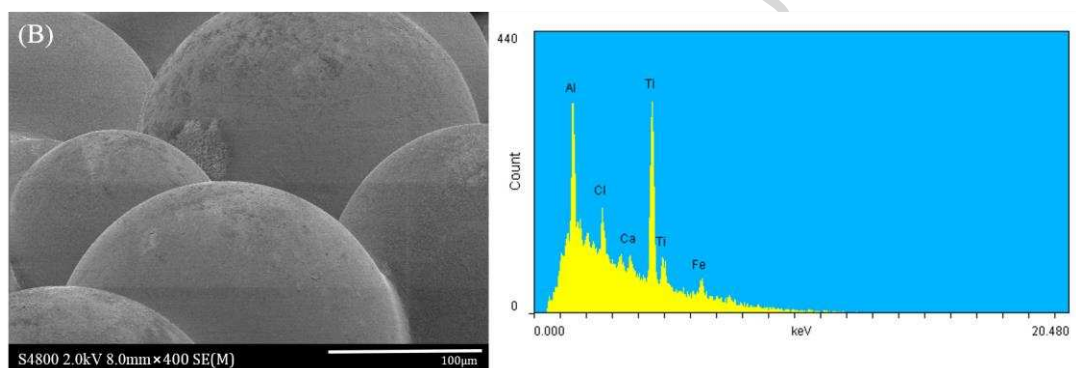
Fig. 4B
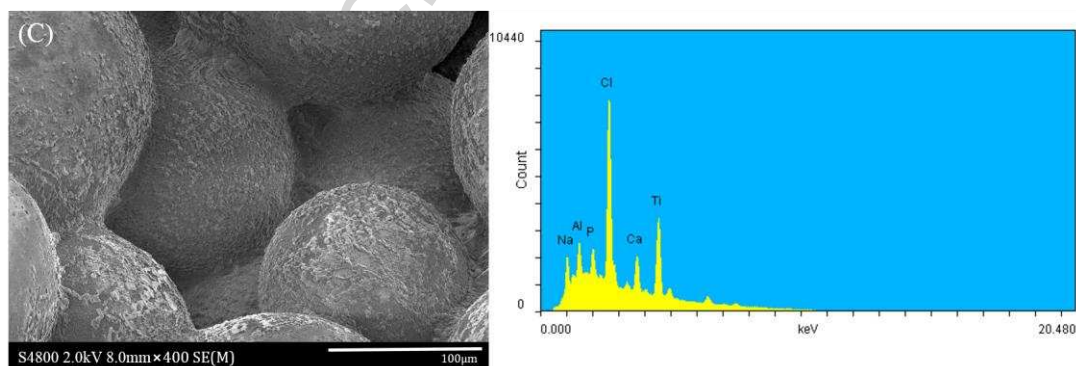
Fig. 4C
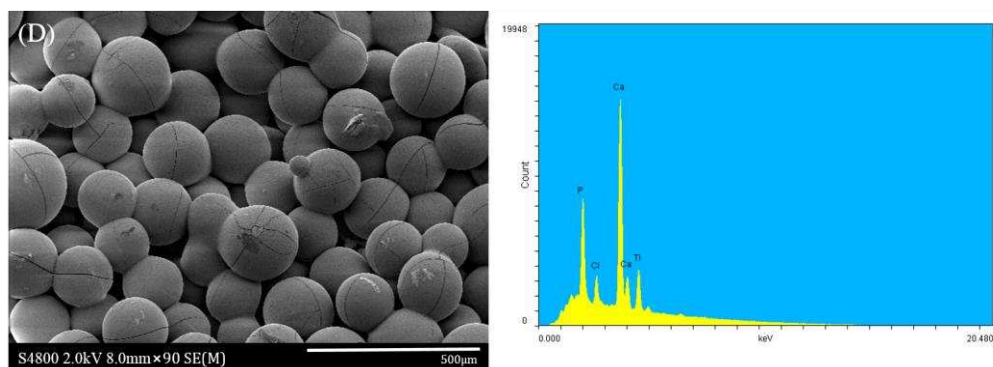
Fig. 4D
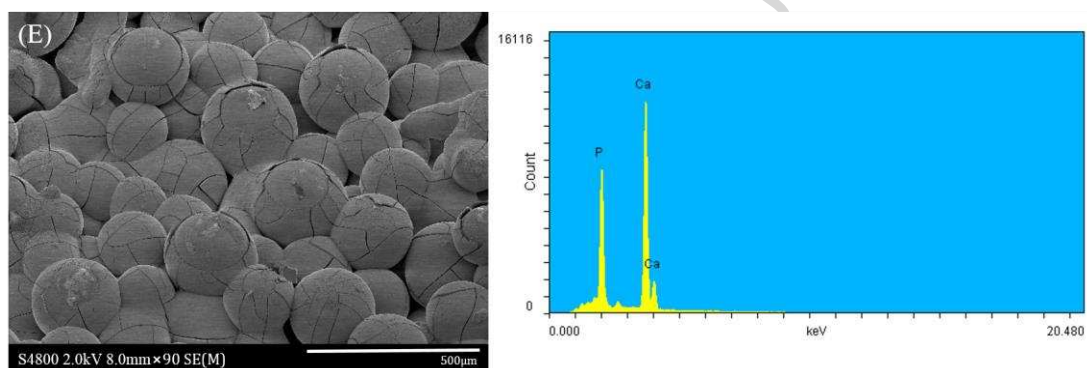
Fig. 4E
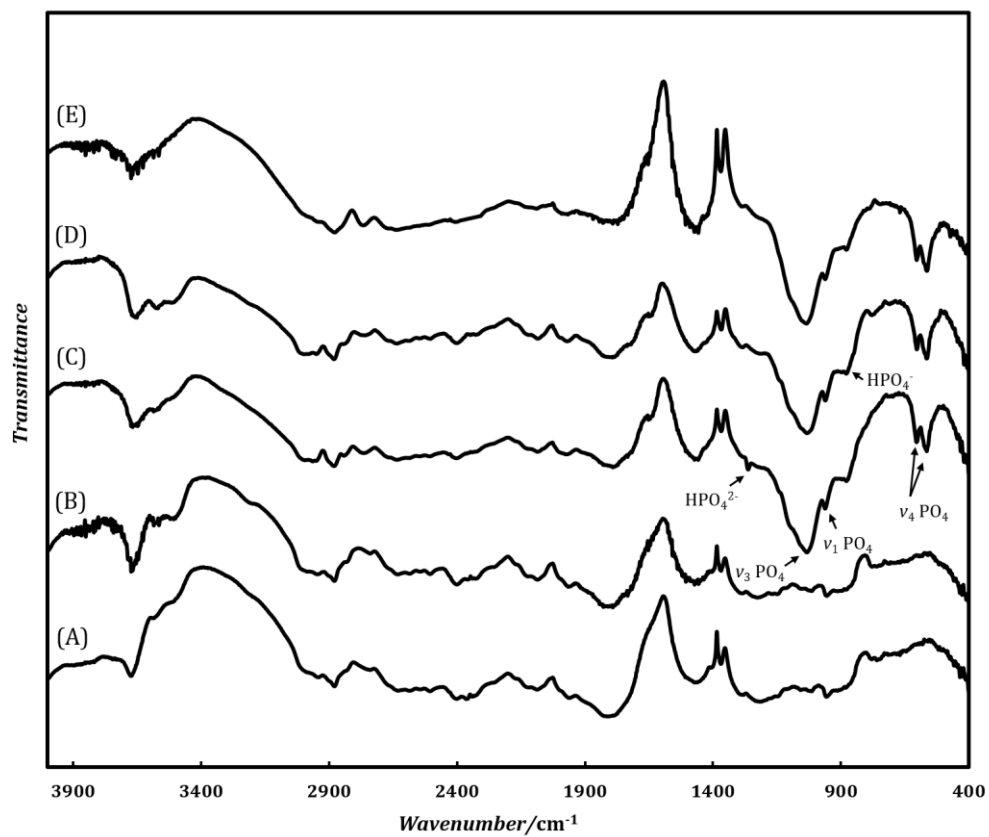
Fig. 5
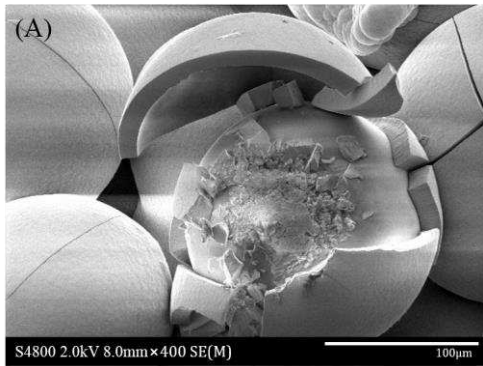
Fig. 6A
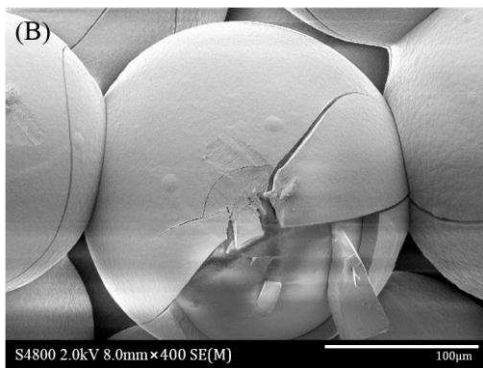
Fig. 6B
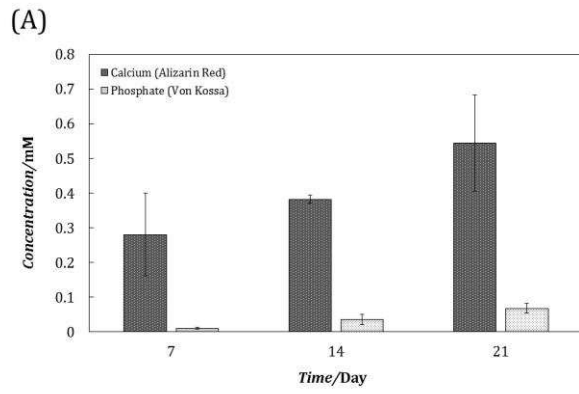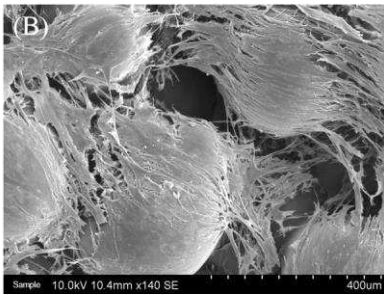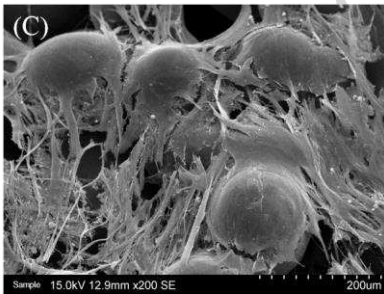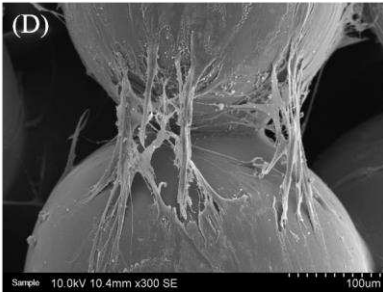

Fig. 6C

Fig. 6D
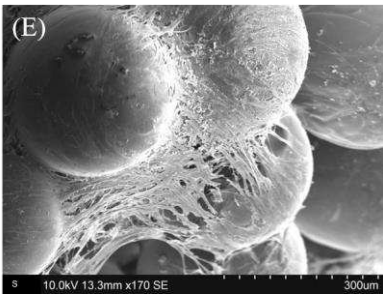
(A)
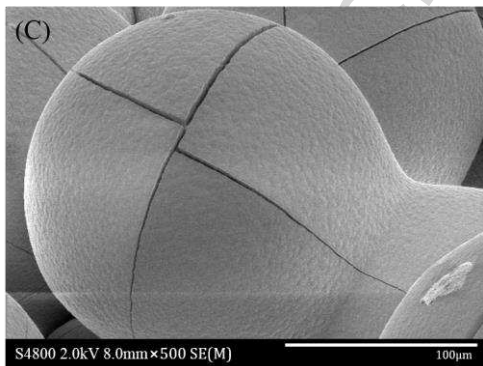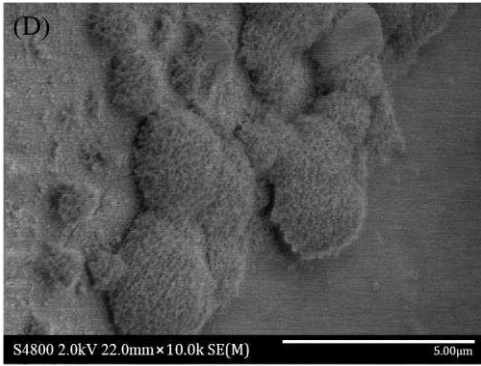
Fig. 7A

Fig. 7B
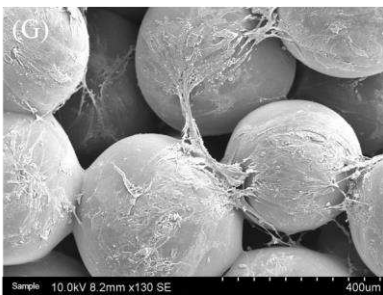

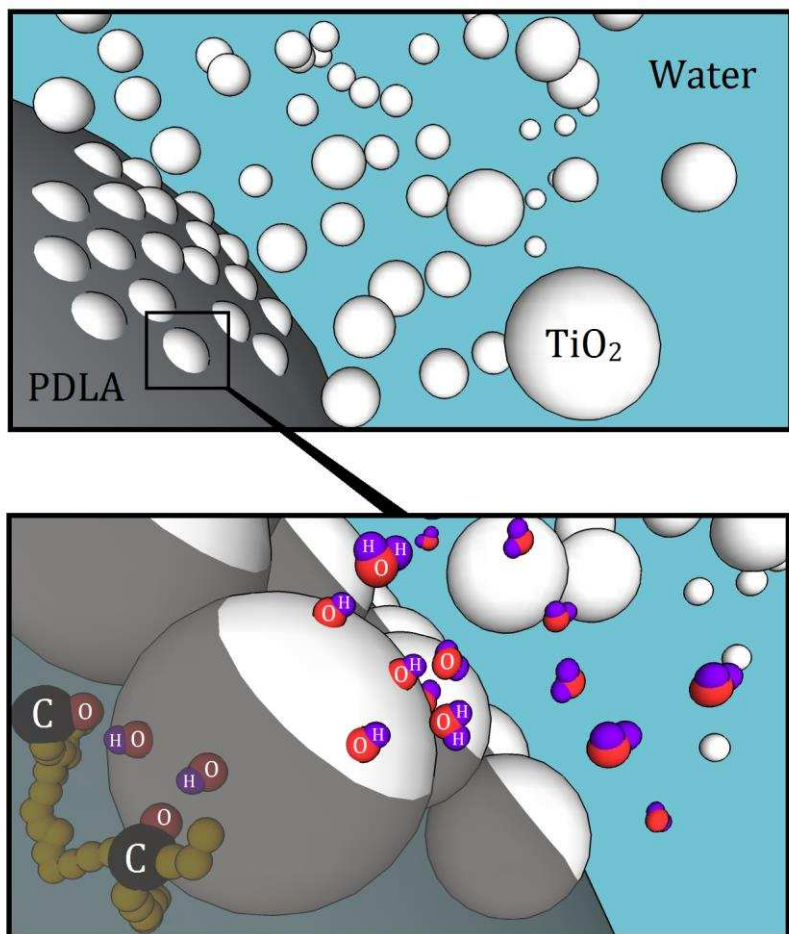Fig. 7C

Fig. 7D

Fig. 7E
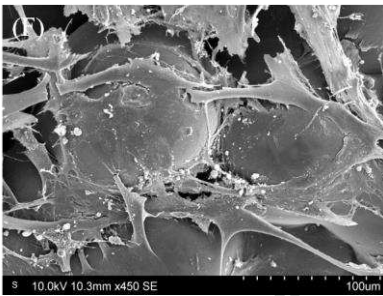
Fig. 7F

Fig. 7G

Fig. 8

Graphical Abstract

In the present study, we introduce an emulsification method to prepare solvent-free microspheres of PLA using TiO_2 nanoparticles as particulate emulsifier. A modified microsphere sintering method is also presented in order to fabricate porous tissue engineering scaffolds with controlled pore size. Both immersion in Simulated Body Fluid and osteoblast culture show progressive calcium phosphate mineralization on the scaffolds.